Journal of Power Sources 193 (2009) 203–215

Contents lists available at ScienceDirect

Journal of Power Sources

journal homepage: www.elsevier.com/locate/jpowsour

Simulation of thermal stresses in anode-supported solid oxide fuel cell stacks. Part I: Probability of failure of the cells

Arata Nakajo*, Zacharie Wuillemin, Jan Van herle, Daniel Favrat

Laboratoire d'Energétique Industrielle (LENI), Institut de Génie Mécanique, Ecole Polytechnique Fédérale de Lausanne, 1015 Lausanne, Switzerland

ARTICLE INFO

Article history:
Received 7 October 2008
Received in revised form 1 December 2008
Accepted 9 December 2008
Available online 24 December 2008

Keywords:
Solid oxide fuel cell
Planar
Thermal stresses
Model
Cell cracking
Weibull

ABSTRACT

Structural stability issues in planar solid oxide fuel cells arise from the mismatch between the coefficients of thermal expansion of the components. The stress state at operating temperature is the superposition of several contributions, which differ depending on the component. First, the cells accumulate residual stresses due to the sintering phase during the manufacturing process. Further, the load applied during assembly of the stack to ensure electric contact and flatten the cells prevents a completely stress-free expansion of each component during the heat-up. Finally, thermal gradients cause additional stresses in operation.

The temperature profile generated by a thermo-electrochemical model implemented in an equation-oriented process-modelling tool (gPROMS) was imported into finite-element software (ABAQUS) to calculate the distribution of stress and contact pressure on all components of a standard solid oxide fuel cell repeat unit.

The different layers of the cell, i.e. anode, electrolyte, cathode and compensating layer were considered in the analysis by using the sub-modelling capabilities of the finite-element tool. Both steady-state and dynamic simulations were performed, with an emphasis on the cycling of the electrical load. The study includes two different types of cells, operation under both thermal partial oxidation and internal steam-methane reforming and two different initial thicknesses of the air and fuel compressive sealing gaskets.

The results generated by the models are presented in two papers: Part I, focuses on the assessment of the risks of failure of the cell, which was performed by Weibull analysis, while the issues related to the other components are discussed in Part II.

Only the anode support contributed to the probability of failure, since the other layers underwent compressive stresses independently of the operating conditions. The cell at room temperature after the reduction procedure was revealed as a critical case. Thermal gradients and the shape of the temperature profile generated during transient operation induced high probabilities of failure. The computed reliability is incompatible with commercialisation, but the scatter induced by the experimental data covers several orders of magnitude. Alternatively, the computed required strength of the anode material to fulfil a probability of failure of 10^{-2} in a 50-cells stack during steady-state operation appears achievable. Finally, extreme care is required when using the maximum thermal gradient or temperature difference over the SRU as an indicator for cell cracking.

1. Introduction

The solid oxide fuel cell (SOFC) is a direct energy conversion device, which allows the production of electricity with high efficiency while maintaining pollutant emissions at a low level. Prototypes have successfully proven their ability to achieve these aims. However, the SOFC technology faces many challenges when it comes to commercialisation, since costs reductions and extended lifetime are required. Under steady-state operation, failures of the SOFC stack arise from the degradation of the materials, which is induced by the high temperature and aggressive environment. In addition, in a system in operation, failure of auxiliary components can cause harmful conditions on the SOFC stack such as reduction–oxidation (redox) cycle, which is a well-known cause of failure or strong degradation of the cell performance in the best case [1,2].

The SOFC field is characterised by a strong coupling of the phenomena. The efforts to increase the reliability of SOFC components cover overlapping research fields. In particular, mechanical issues will affect the thermo-electrochemical behaviour of a planar SOFC stack, through for instance local loss of electrical contact or gas tightness. These issues may themselves arise from the modifica-

* Corresponding author. Tel.: +41 21 693 35 05; fax: +41 21 693 35 02.
E-mail addresses: arata.nakajo@epfl.ch (A. Nakajo), zacharie.wuillemin@epfl.ch (Z. Wuillemin), jan.vanherle@epfl.ch (J. Van herle), daniel.favrat@epfl.ch (D. Favrat).

0378-7753/$ – see front matter © 2009 Elsevier B.V. All rights reserved.
doi:10.1016/j.jpowsour.2008.12.050

Nomenclature

A	active area per unit volume ($m^2\,m^{-3}$)
ASR	area specific resistance ($\Omega\,m^{-2}$)
B_o	permeability in the porous medium (m^2)
c_t	total molar concentration ($mol\,m^{-3}$)
c	heat capacity ($J\,kg^{-1}$)
d	particle diameter (m)
$\mathcal{D}^e_{iM}$	effective Knudsen diffusivity of species i in porous medium ($m^2\,s^{-1}$)
$\mathcal{D}^e_{ij}$	effective bulk diffusivity of binary pair in porous medium ($m^2\,s^{-1}$)
E_a	activation energy ($J\,mol^{-1}$)
F	Faraday's constant ($C\,mol^{-1}$)
h	thickness (m)
h_c	convection heat transfer coefficient ($W\,m^{-2}\,K^{-1}$)
H	gas enthalpy ($J\,kg^{-1}$)
i_o	exchange current density ($A\,m^{-2}$)
i_t	transfer current density ($A\,m^{-2}$)
j	current density ($A\,m^{-2}$)
k_o	kinetic constant ($A\,K^{-1}\,m^{-2}$)
K	experimental permeability coefficient
l	distance between the particles (m)
M_i	molecular weight of species i ($kg\,mol^{-1}$)
N_i	molar flux of species i ($mol\,m^{-2}\,s^{-1}$)
p	pressure (Pa)
$\dot{Q}$	volumetric rate generated thermal energy ($W\,m^{-3}$)
r	reaction order, dimensionless
R	universal gas constant, 8.314 ($J\,mol^{-1}\,K^{-1}$)
$\Re_i$	rate of production of species i ($mol\,m^{-3}\,s^{-1}$)
$\Re_i^m$	rate of production of species i due to electrochemical reaction ($kg\,m^{-3}\,s^{-1}$)
T	temperature (K)
T_{ref}	reference temperature, 873 (K)
u	gas velocity ($m\,s^{-1}$)
V	potential (V)
x_i	mole fraction of species i, dimensionless

Greek letters

α	symmetry coefficient, dimensionless
η	overpotential (V)
λ	thermal conductivity ($W\,m^{-1}\,K^{-1}$)
μ	viscosity (Pa s)
ρ	density ($kg\,m^{-3}$)
ρ^{eff}	effective resistivity in the mixed ionic and electronic conductor ($\Omega\,m$)
σ	electrical conductivity ($S\,m^{-1}$)
ω	mass fraction of species i, dimensionless

Indices

a	anodic
c	cathodic
CT	charge transfer
el	electronic
g	gas, either air or fuel
io	ionic
s	solid

Superscripts

an	anode
atm	one bar, 1.01325 (Pa)
cath	cathode
elect	electrolyte
eq	equilibrium
red	anode support in reduced state
Th	thermal

Acronyms

0s	zero-stress temperature
INI	analysis steps during initialisation of the contact simulations
IV	analysis steps during current–voltage characterisation
GDL	gas diffusion layer
LS	analysis steps during the variation of the electrical load
MIC	metallic interconnect
MIEC	mixed ionic and electronic conductor
RT	room temperature
SH	analysis steps during the rapid electrical load shutdown and cool-down
SMR	steam-methane reforming
TPOX	thermal partial oxidation

tion of the temperature profile induced by the degradation of the cell performance. As a consequence, experiments usually end up by the mechanical failure of one of the components. Typical mechanical issues of interest are cell fracture, loss of gas tightness of the gas compartments and plastic deformation and buckling of the metallic interconnects (MIC).

There are several causes of stresses in a cell. First, the sintering phase during the manufacturing process induces residual stresses due to the mismatch between the coefficients of thermal expansion (CTE) of the materials of the cell. Therefore, the mechanical load applied during the assembly of the stack has to account for the curvature of the cell in order to ensure both the electrical contact and the gas tightness of the compartments if compressive sealing gaskets are used. Then, once loaded, friction prevents a stress-free expansion of each component during heat-up and operation. The last manufacturing step of a SOFC stack is usually the reduction procedure of the anode, which takes place when the fuel is fed for the first time. The mechanical properties of the anode support change and influence the cell curvature. Thus the stresses in a stack after a thermal cycle and after the assembly are expected to be different. Finally, the temperature profile during operation causes additional stresses in all layers of the repeat unit. The features of the temperature profile during operation obviously depend on the stack design as well as on the control strategy, flow configuration and fuel composition. Zones of relatively high temperature may induce buckling and will cause a redistribution of the assembly load, which might lead to a partial loss of electrical contact and applied pressure on the gaskets. The latter phenomena can also arise from the CTE mismatch of adjacent components, typically gasket and gas diffusion layer (GDL), if the assembly load is not sufficient. Hence, the temperature profile has to be known with accuracy and the reliability of the thermo-electrochemical model is paramount.

Only few studies have been carried out on stresses in SOFC. Yakabe et al. [3,4] were among the first to address both the thermal and chemical stress issues, by coupling thermo-electrochemical models with structural analysis. Experimental work using the X-ray diffraction method was carried out to compare the computed and actual residual stresses in the electrolyte of an anode-supported cell [5,6]. Selimovic et al. [7] considered the effect of the choice of either metallic or ceramic interconnectors on the stresses through the differences in computed temperature profiles, during operation, heat-up and shutdown procedures. Lin et al. [8] developed a finite-element model of a 5-cell stack meshed with linear shell ele-

ments, which included all components of their SOFC stacks. Plastic deformation was considered. The probability of survival was monitored during transient operation for tubular SOFC [9]. Nevertheless, most studies on standard repeat units (SRU) or stacks did not consider the effect of the residual stress, i.e. stress state and change of curvature of the cell, thermal buckling nor loss of either electrical contact or gas tightness.

The data on mechanical properties of the relevant components is currently increasing but remains sparse, in particular when the temperature dependence is regarded. The 2-parameter Weibull analysis was widely accepted to characterise the ceramic components [10–12]. Some key parameters are still difficult to find in literature, due to the difficulty in manufacturing or testing. A typical example is the properties of the reduced anode material at high temperature due to the need of a reducing atmosphere above approximately 673 K. The cathode materials are studied extensively in dense state [13,14], but very little information on the properties of porous cathode is available [11]. Engineering data on the properties of alloys used as MIC material is available [15], even though detailed constitutive models could not be found. Metallic foams can be used as GDL. Extensive research has been carried out in the field, even though not specifically on SOFC materials [16]. The mechanical behaviour of compressive sealant materials used as gaskets is complex and has not been studied extensively, even though their performance, measured as a leak flux has been estimated. Refs. [17,18] showed that their compressive behaviour follows non-linear and differentiated loading and unloading paths, together with plasticity. The properties were found to change significantly during the first loading cycles. Creep at high temperature was observed as well.

Thermo-electrochemical models are more common, and are based on the knowledge acquired with micro-modelling of electrodes [19–21]. Studies underscored the need for refined models with dynamic capabilities to simulate the conditions a real stack will have to face during operation [22].

The framework of the present study is the FP6 European project FLAMESOFC, which aims at developing a cogeneration system foreseen for domestic application. A particular feature of the project is a thermal partial oxidation (TPOX) reformer. The 2.5 kWe class stack design was developed at LENI-EPFL, in collaboration with HTceramix-SOFCPower. The manifold of the stack is external and can accommodate both co- and counter-flow configurations. The active area is 198.5 cm^2.

The aim of the present work is to study the mechanical issues in a standard SOFC repeat unit with an anode-supported cell during the typical phases of its service, i.e. assembly, heat-up, current–voltage (IV) characterisation, dynamic operation, load shutdown and cool-down. The approach consists in importing into finite-element software the temperature profile computed by a reasonably detailed and experimentally calibrated thermo-electrochemical model of SRU with dynamic capabilities. The results are presented in two papers: the present one (Part I) focuses on the description of the modelling approach, including the thermo-electrochemical model and the computation of the probability of failure of the cells, while the issues related to the other components of the SRU, i.e. loss of gas tightness and/or electrical contact and plastic deformation and thermal buckling of the interconnect are explored in Part II [23]. The accuracy of the thermo-electrochemical model is of paramount importance for the reliability of the computation of the stresses. Its modelling approach is presented but the results are not detailed, which will be done elsewhere. This model is then coupled with a structural model, which considers all components of the SRU and models their interaction through contact simulations. The assessment of structural failure of the cell is handled by the widely used Weibull analysis and performed on the stress profiles computed by a detailed cell sub-model, which nodes are driven by the SRU contact model, for different operating conditions, types of cells and initial thicknesses of the air and fuel gaskets. Data from the literature on the strength of the materials is used first, then requirements on the strength of the material of the most critical component, the anode support, are set to fulfil a fixed probability of failure in a 50-cell stack.

2. Modelling

2.1. Thermo-electrochemical model

The capabilities of an existing thermo-electrochemical model described by Larrain et al. [24] were extended. The equations were implemented in gPROMS, an equation-oriented process-modelling tool [25]. Model evolutions include the adaptation of the geometry to the FLAMESOFC stack, the modifications of the conservation of species to handle internal steam-methane reforming, the implementation of proportional integral derivative (PID) controllers and an in-depth revision of the electrochemical model. The geometry and components of the SRU are depicted in Fig. 1. The species on the fuel side are restricted to H_2, H_2O, CO, CO_2, CH_4 and N_2.

The SRU is spatially discretised in the in-plane direction and coupled to a local one-dimensional electrochemical model, which is discretised through the thickness of the cell. Thus, averaged values for the properties of the solid structure are used. The validity and limitations of this assumption were tested in the early stage of development of the model [24] and tested against a one-dimensional model of a large stack. On the other hand, the variables of the electrochemical model, such as molar fluxes of gas species, reaction rates, ionic and electronic current densities include the cell thickness as local third dimension.

The model is not fully dynamic in term of species transport and heat transfer, since only thermal inertia of the solid structure is accounted for. The energy conservation of the solid is calculated as

$$\lambda_s \nabla^2 T_s + \dot{Q}_s = \rho_s c_s \frac{dT_s}{dt} \quad (1)$$

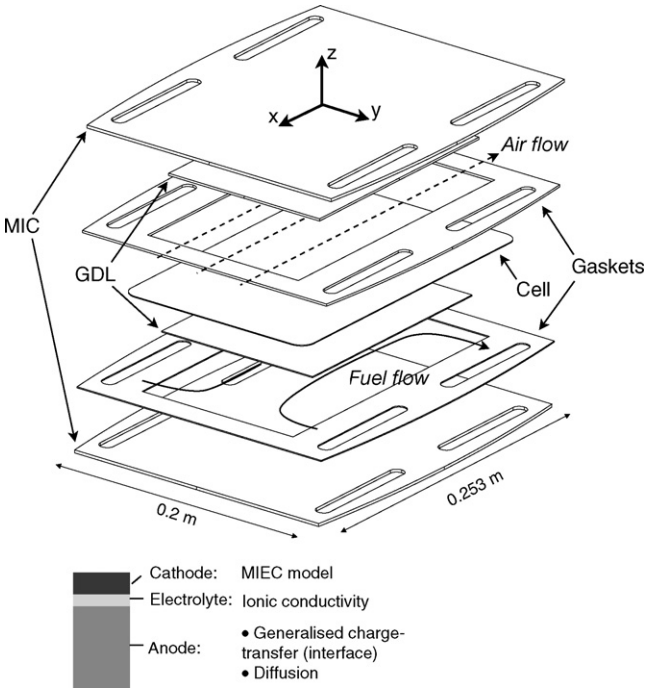

Fig. 1. Top: geometry and components of the standard repeat unit, indicated flow direction holds for co-flow configuration. Bottom: overview of the contributions considered in the electrochemical model at the cell level.

Boundary conditions include the heat losses to the environment through the insulation. Heat exchange by radiation between the stack and its surrounding is modelled in a simplified manner, i.e. each node is coupled to an equivalent front node of the insulation. The exchange with above/underneath and front/rear nodes is neglected [26].

The conservation of energy of gases as well as the conservation of species accounts for variations of gas densities:

$$\rho_g \mathbf{u}_g \cdot \nabla H_g + H_g \sum \Re_i^m = \dot{Q}_g \tag{2}$$

$$\rho_g \mathbf{u}_g \cdot \nabla \omega_i + \omega_i \sum \Re_i^m = \frac{M_i N_i^{\text{GDL-an/cath}}}{h_c} \tag{3}$$

The exchange by convection between the gases and the solid structure as well as the thermal energy released by the chemical and electrochemical reactions are embedded in the rate of volumetric thermal energy generated $\dot{Q}_s$. The energy released by the chemical reactions is computed from the balance of species at the anode–gas interface.

The gas velocity is described by the common Darcy law, which is solved along with the mass conservation:

$$\mathbf{u}_g = -\frac{K}{\mu}\nabla p \tag{4}$$

$$\nabla \cdot (\rho_g \mathbf{u}_g) = \sum \Re_i^m \tag{5}$$

The core of the model is the electrochemical model. It considers both ohmic and non-ohmic losses (Fig. 1, bottom). The first contribution includes the ionic resistance of the electrolyte [27], the electrical resistance of the MIC and a small electronic conductivity of the electrolyte, which induces a small leakage current [24]. Thin electrolytes used in anode-supported cells show a higher resistance than thick ones relative to their thickness. Fleig et al. [28] attributed this increase in resistance to current constriction, due to the uneven interface between the dense electrolyte and the porous electrodes. The interpolated relation they proposed could satisfactorily reproduce finite-element calculations and is used in the present work:

$$\text{ASR}_{\text{io}}^{\text{elect}} = \frac{h^{\text{elect}}}{\sigma_{\text{ion}}^{\text{elect}}} + \frac{l}{\sigma_{\text{ion}}^{\text{elect}}}\left(\frac{(l/d)-1}{(d/l)+1}\right) \tag{6}$$

More computing time is spent on the non-ohmic losses. On the anode side, the dusty-gas model [29] is solved in one-dimension through the anode support, along with the equation of continuity. The water-gas-shift reaction is assumed at equilibrium until the interface between the anode and the electrolyte, whereas methane steam-reforming is computed according to the kinetic approach of Achenbach and Riensche [30], as the species diffuse toward the interface between the electrolyte and the anode. Hence the system of equations to solve is as follows:

$$-\frac{d}{dz}x_i - \frac{x_i}{p}\frac{d}{dz}p - x_i\frac{B_o}{\mu \mathcal{D}_{iM}^e}\frac{d}{dz}p = \sum_{j=1,j\neq i}^{n}\frac{x_j N_i - x_i N_j}{c_t \mathcal{D}_{ij}^e} + \frac{N_i}{c_t \mathcal{D}_{iM}^e} \tag{7}$$

$$\frac{d}{dz}p = -\frac{\sum_{i=1}^{n}\frac{N_i}{\mathcal{D}_{iM}^e}}{\left(\frac{1}{RT}\right)+\left(\frac{B_o}{\mu}\right)\sum_{i=1}^{n}\frac{x_i}{\mathcal{D}_{iM}^e}} \tag{8}$$

$$\frac{d}{dz}N_i = \Re_i \tag{9}$$

$$z = h^{\text{an}}: \quad N_{\text{H}_2} = \frac{j}{2F}, \quad N_{\text{H}_2\text{O}} = -\frac{j}{2F}, N_i = 0$$
$$\text{for } i = \text{N}_2, \text{CH}_4, \text{CO}, \text{CO}_2 \tag{10}$$

$$z = 0: \quad x_i^{\text{an}} = x_i^{\text{GDL}} \quad p = p^{\text{atm}} \tag{11}$$

Currently only hydrogen is electrochemically converted at the electrolyte-anode interface, according to the relation from Bessler [31]:

$$i_t^{\text{an}} = i_o^{\text{an}} x_{\text{H}_2}^{r1} x_{\text{H}_2\text{O}}^{r2}\left[\exp\left(\alpha_a^{\text{an}}\frac{F}{RT}\eta_{\text{CT}}^{\text{an}}\right) - \exp\left(-\alpha_c^{\text{an}}\frac{F}{RT}\eta_{\text{CT}}^{\text{an}}\right)\right] \tag{12}$$

The gas compositions at the interface are computed from the dusty-gas model. The dependence on temperature of the exchange current is considered:

$$i_o^{\text{an}} = T \cdot k_o^{\text{an}} \cdot \exp\left[-\frac{E_a^{\text{an}}}{R}\cdot\left(\frac{1}{T}-\frac{1}{T_{\text{ref}}}\right)\right] \tag{13}$$

On the cathode side, a model of mixed-ionic and electronic conductor solves the charge balance along with the mass transport [19–21]. The charge balance is described by the following system of equations,

$$\frac{d}{dz}V_{\text{ion}} = -\rho_{\text{ion}}^{\text{cath}} j_{\text{ion}}^{\text{cath}} \tag{14}$$

$$\frac{d}{dz}V_{\text{el}} = -\rho_{\text{el}}^{\text{cath}} j_{\text{el}}^{\text{cath}} \tag{15}$$

$$\eta_{\text{MIEC}}^{\text{cath}} = (V_{\text{ion}}^{\text{eq}} - V_{\text{el}}^{\text{eq}}) - (V_{\text{ion}} - V_{\text{el}}) \tag{16}$$

$$\frac{d^2}{dz^2}\eta_{\text{MIEC}}^{\text{cath}} = A \cdot (\rho_{\text{el}}^{\text{eff}} + \rho_{\text{io}}^{\text{eff}}) \cdot i_t^{\text{cath}} \tag{17}$$

$$z = 0: \quad j_{\text{ion}} = 0 \quad j_{\text{el}} = 0 \tag{18}$$

$$z = h^{\text{cath}}: \quad j_{\text{ion}} = j \quad j_{\text{el}} = 0 \tag{19}$$

whereas the Eqs. (20)–(22) are solved for the mass transport:

$$\frac{p}{RT}\frac{d^2}{dz^2}x_{\text{O}_2} = \frac{1}{4F\mathcal{D}_{\text{O}_2-\text{N}_2}^e} A \cdot i_t^{\text{cath}} \tag{20}$$

$$z = 0: \quad x_i^{\text{cath}} = x_i^{\text{GDL}} \tag{21}$$

$$z = h^{\text{cath}}: \quad j_{\text{ion}} = j \quad j_{\text{el}} = 0 \tag{22}$$

The coupling between both systems is performed by the transfer current, which is described following the approach of van Heuveln and Bouwmeester [32]:

$$i_t^{\text{cath}} = i_o^{\text{cath}} x_{\text{O}_2}^{r3}\left[\exp\left(\alpha_a^{\text{cath}}\frac{F}{RT}\eta_{\text{MIEC}}^{\text{cath}}\right) - \exp\left(-\alpha_c^{\text{cath}}\frac{F}{RT}\eta_{\text{MIEC}}^{\text{cath}}\right)\right] \tag{23}$$

$$i_o^{\text{cath}} = T \cdot k_o^{\text{cath}} \cdot \exp\left[-\frac{E_a^{\text{cath}}}{R}\cdot\left(\frac{1}{T}-\frac{1}{T_{\text{ref}}}\right)\right] \tag{24}$$

The values of the apparent reaction order on oxygen partial pressure and the symmetry factor depend on the assumptions on the mechanisms and in particular the choice of the rate limiting step. The charge-transfer on adsorbed oxygen was considered for the present work, which yields $r_3 = 3/8$, $\alpha_a = 3/2$ and $\alpha_c = 1/2$ [21,32].

Values are available in literature for the different above-listed parameters. They can vary within more or less large ranges, which reflect for instance material, morphological or experimental variations. Thus, fitting parameters are required to describe precisely the behaviour of a SRU. In the present study, the parameters were calibrated on experimental data [33] using the parameter estimation capabilities of gPROMS. The final computation was performed on 25,000 measurements points on an anode-supported cell with LSCF cathode, including different temperatures, fuel and oxidizer fluxes and compositions and flow configurations. The parameter estimation runs were performed with a one-dimensional version of the

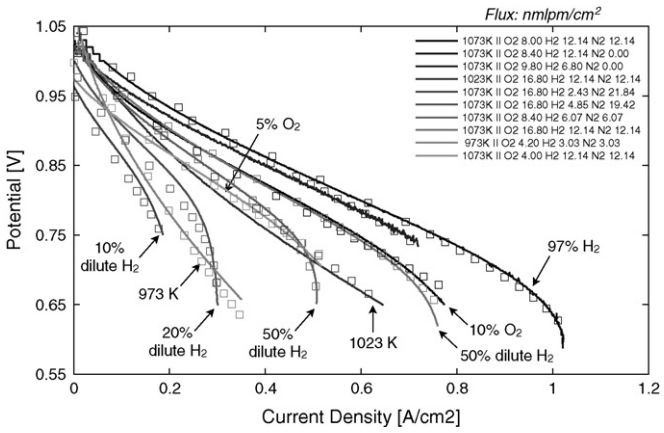

Fig. 2. Comparison of simulated and measured current–voltage characteristics. Experimental data from P. Metzger (DLR).

model, coupled to the electrochemical model. Fig. 2 depicts a sample of the calibration of the model on experimental current–voltage characteristics (IV). The agreement is satisfactory. Part of the discrepancy can be attributed to the time period of 400 h over which the measurements were spread.

Finally, three PIDs, a standard feature included in gPROMS, control (i) the air outlet temperature by the air flow, (ii) the cell potential by the fuel flow and (iii) the electrical power by the current density. The PID parameters were coarsely determined using the empirical Ziegler-Nichols method and tuned on the one-dimensional version of the thermo-electrochemical model. Here, the aim is not to propose an efficient control strategy, but rather to identify possible harmful conditions that can be induced by a simple and unrefined control.

2.2. Mechanical model

2.2.1. Model of standard repeat unit for contact simulations

The uncoupled linear thermo-elastic theory is used for the computation of the stresses. The three-dimensional computer-aided design (CAD) drawings were imported, assembled and meshed in ABAQUS [34], a numerical tool based on the finite-element method. A combination of three-dimensional reduced linear (C3D8R) and second-order elements (C3D20R) are used in combination to second-order (S8R) shell elements and linear gasket elements (GK3D8R). The contact algorithm of ABAQUS is used to compute the interaction between the components.

The main assumptions of the contact model are

- Small deformations are assumed, i.e. geometric non-linearity is not considered.
- The surface-to-surface contact discretisation is used to limit the occurrence of interpenetrations of the surfaces.
- The small-sliding tracking method for contact pairs available in ABAQUS allows reducing the computing time. Indeed, The algorithm does not have to monitor slave nodes for interaction with the whole master surface, since a local tangent plane of the master surface is defined for each slave node. The underlying assumptions holds for the present case, since the relative motion of the components of the SRU is expected to be small.
- Softened contact is assumed between all components for the normal behaviour. Indeed, all contact pairs involve either a metallic foam or a gasket, which surfaces are usually uneven. In such case, it is expected that the pressure is progressively transmitted between the surfaces, even though no measurement could be found. Hence, default values were used. The same applies for the tangential behaviour, where no measurements of the friction coefficients could be found: a default value of 0.2 was used for all interactions.
- The choice of 2.5 mm-thick MICs prevents any thermal buckling (cf. 3.1 Part II [23]). Thus the middle plane through the thickness of each MIC is constrained to remain flat. Rotations are allowed only around the *y*-axis (see Fig. 1), since the *x*-symmetry is assumed to reduce the memory requirements. Therefore, the computations are performed for only one half of a repeat unit, which is believed to be representative of the conditions within a stack.
- The assembly load of 5000 N is transmitted to the SRU by an analytical rigid surface. This value was kept constant for the present study, even though it can be easily varied.
- A fairly dense mesh of second-order elements is required for the cell, since the cathode covers only partially the cell. This detailed mesh of the cell could not be used for the contact analysis, due to memory limitations. Therefore, a coarser version of the mesh of the cell, which neglects the cathode, is used in the SRU contact model. Indeed, the cathode has the lowest Young modulus hence the lowest influence on the cell curvature. To overcome this limitation, the sub-modelling capabilities of ABAQUS are used to impose the boundary conditions computed by the SRU contact model to the detailed cell sub-model. The information flow and interactions between the gPROMS and the two ABAQUS models are depicted in Fig. 3. The importation of the temperature profile is performed for each layer of the ABAQUS mesh. All pre- and post-processing tasks are performed by MATLAB [35] rou-

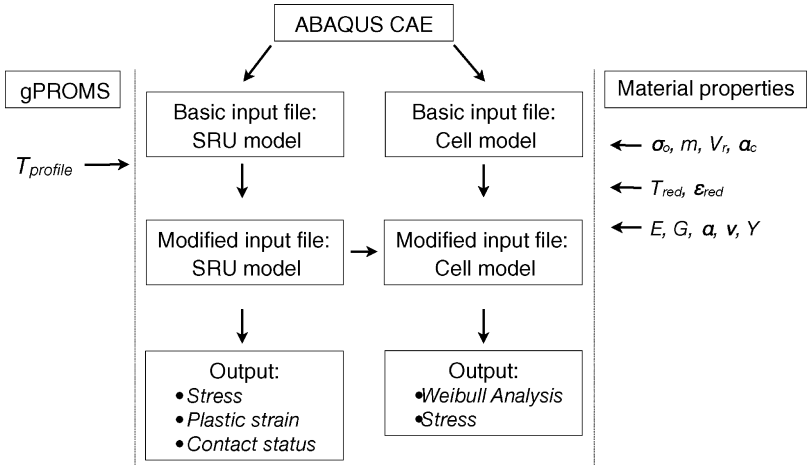

Fig. 3. Information flow between the models.

Table 1
Mechanical properties of the components of the standard repeat unit [5–13,15–18,37–39,41].

		Porosity (%)	Layer thickness (m)	Reduction strain (%)	Zero stress temperature (K)	Young's modulus (GPa)	Poisson's coefficient	Coefficient of thermal expansion ($\times 10^{-6}\,K^{-1}$)	Elastic limit (MPa)	Characteristic strength (MPa)	Weibull modulus
Cathode (LSM)	RT HT	0.36	35E−6	–	1323[a]	29.7[b]	0.25	11.7	–	52[b] 75[b]	6.7[b] 3.7[b]
Electrolyte (YSZ)	RT HT	0	7E−6	–	1473	215 185	0.317	10.2[c]	–	232 154	5.7 8.6
Anode (NiO-YSZ)	–	0.17	542E−6	–	1473	131[b]	0.317	12.2[c]	–	97 (86,110)	6.8 (4.3,9.8)
Anode (Ni-YSZ)	–	0.36	542E−6	0.07	1473	69[b]	0.317	12.6[c]		79 (73,85)	7 (4.8,10.1)
Compensating layer (YSZ)	RT HT	0	4E−6	–	1473	215 185	0.317	10.2[c]	–	232 154	5.7 8.6
GDL anode (Ni)	RT HT	5w	1E−3	–	–	0.154[d] 0.114[d]	0.3	16.2[c]	0.63[d] 0.188[d]	–	–
GDL cathode	RT HT	5w	2E−3	–	–	0.147[d] 0.114[d]	0.3	11.9[c]	1.3[d] 0.88[d]	–	–
Gasket (Flexitallic 866)	–	na	1–2E−3	–	–	0.019[e]	0	13.9	–	–	–
Metallic parts (Crofer22APU)	RT HT	0	0.5–2E−3	–	–	216 71	0.3	11.9[c]	248 35	–	–

[a] Assumed values.
[b] 0.33 porosity.
[c] Value from RT to 1073 K. Temperature-dependent values implemented in the model.
[d] Computed from dense material.
[e] Through the thickness: Full non-linear pressure-closure relation.

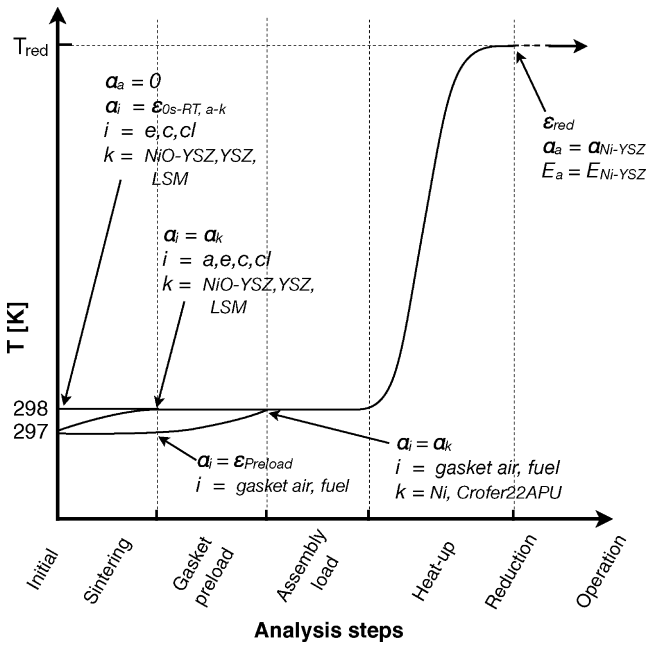

Fig. 4. Initialisation sequence for the contact simulations, i: layer of component, a: anode, e: electrolyte, c: cathode, cl: compensating layer, k: material.

tines. Finally, the stress profiles computed by the cell sub-model are used to compute the probabilities of failure for each layer of the cell. The reference volumes during ring-on-ring experiments are computed in compliance with the C1499-04 ASTM standard. Only tensile stresses contribute to the probability of failure in the Weibull analysis, even though compressive stresses may induce failure through other mechanisms such as delamination [2]. The computation is performed according to [9].

- Data from literature was used for the mechanical properties (Table 1).

Mechanical loading, heat-up and reduction are necessary steps before the simulation of the operation of the stack. They imply a modification of the properties of the materials. Fig. 4 shows the initialisation process. The modelling procedure used for the sintering, gasket preload and reduction steps are detailed hereafter.

First, the sintering phase is handled by setting artificial CTEs in the electrolyte, anode-compensating layer [40] and cathode. The values of the artificial CTEs correspond to the mismatch strain between the oxidized anode and the considered layer (cf. indices *i* in Fig. 4) from the zero stress temperature (0s) to room temperature (RT). The value of the zero stress temperature is of the highest importance for the determination of the magnitude of the residual stresses in the cell. It differs from the sintering temperature since the creep strain rate is not negligible at temperatures above the zero stress temperature (usually around 1473 K) during the manufacturing process, typically $\geq$1573 K [10]. The values depend on the material and are listed in Table 1. The CTE of the anode equals to zero during this step. Thus, the sintering phase correspond to an increase of 1 K of the cell. The actual CTE are then reinserted in the model for the subsequent steps.

Second, the thickness of the gaskets relative to the GDL can differ before the assembly. This is a design variable, which can be used to control the distribution of the assembly load on the SRU. An additional initialisation step is added for this purpose ("gasket preload" step in Fig. 4), where an anisotropic and artificial thermal strain is induced prior to the assembly, in a similar manner to the sintering step.

Finally, the reduction procedure of the anode induces a shrinkage strain and modifies its mechanical properties, i.e. Young's modulus, CTE and strength. The reduction temperature is expected to influence the stresses in the cell by modifying both the reduction strain and the CTE. The discrepancy between the reduction strains reported by several authors [36,41] is very large. Preliminary work showed that the contribution of the change in CTE remains small. A uniform value of 1073 K was used for all computations of the reduction process within this work.

Compressive gaskets usually have a complex behaviour. Gasket elements embedded in ABAQUS uncouple the in-plane and through-the-thickness behaviour. Non-linear, differentiated loading and unloading path together with plasticity are considered for the latter, and the value of the closure, i.e. the effective compression strain ε–ε_{Th}, at maximum pressure is set according to the data from Bram et al. [17].

Engineering stress–strain curves from alloy suppliers [15] were implemented in the model. GDLs made of metallic foam were considered. Gibson and Ashby [16] proposed relations to estimate their properties from the ones of dense materials [15,37].

2.2.2. Investigated cases

Investigated cases differ in cell types, flow configurations, fuel fed into the SRU and initial thicknesses of the gaskets.

Cell suppliers propose different types of cells made of different materials. The most important variations concern the choice of the cathode material. Typical standard cells are made of Ni-YSZ anode, 8YSZ electrolyte and LSM-YSZ cathode. Compensating layers are sometimes added to limit the cell curvature and allow an easier and more precise assembly [40]. Values for dense materials were used for their mechanical properties, even though they are porous in reality, to enable the diffusion of the gas species. Therefore, two different types of cell were considered for the structural analysis:

- C1: anode, electrolyte, LSM cathode
- C2: compensating layer, anode, electrolyte, LSM cathode

Their thickness and mechanical properties are listed in Table 1. The electrochemical performance of C1 and C2 differs from the anode-supported cell with LSCF cathode, on which the electrochemical model was calibrated (cf. Section 2.1). Furthermore, small changes in in-plane conductivities and thermal inertia should be considered. However, all thermo-electrochemical simulations were performed for the LSCF cathode-based cell and used as input for the structural analysis indifferently of the cell type, in order to investigate the issues associated to specific temperature profiles, rather than technological solutions.

The history of a test is of main interest once plastic deformation is considered. The following sequence of structural analysis steps was computed for both co- and counter-flow configurations under both TPOX and internal steam-methane reforming conditions, leading to a set of four thermo-electrochemical cases:

- *Assembly*: sintering and cool-down to room temperature, assembly load at room temperature, heat-up and reduction at a uniform temperature of 1073 K. These steps are referred as INI1-4.
- *IV characterisation*: steady-state computation, gas flows fixed at nominal flow for the full load operating point. Six temperature profiles, ranging from open circuit voltage (OCV) to the end of the current–voltage characterisation were imported into the finite-element tool. The air ratio was set to ensure a maximum temperature in the SRU close to 1100 K. These steps are referred as IV1-6, IV5 corresponding to the nominal point (0.4 A cm^{-2}).
- *Variation of electrical load*: idle conditions (fuel flow: 1.4–3.5 nmlpm cm^{-2}, air ratio: 3–4), nominal load

Table 2
Fixed inlet conditions for the thermo-electrochemical cases.

	Partially pre-reformed methane	TPOX reformate
x_{H_2}	0.263	0.283
x_{H_2O}	0.493	0.060
x_{N_2}	0.000	0.489
x_{CH_4}	0.171	0.000
x_{CO}	0.029	0.125
x_{CO_2}	0.044	0.043
T_{AIR}	973.15	973.15
T_{FUEL}	973.15	973.15

(0.275 W cm^{-2}), part load (0.175 W cm^{-2}), minimum load (0.1 W cm^{-2}), and back to nominal load. Gas flows and current density were controlled by the PIDs, to achieve the desired fuel utilisation (0.7–0.725), air outlet temperature (1100 K) and electrical power, respectively. Nine temperature profiles from the dynamic simulations were selected depending on the value of the thermal gradients and temperature difference over the SRU and imported into the finite-element tool. These steps are referred as LS7-15.

- *Rapid electrical load shutdown*: OCV, fuel flow at minimum allowed value (1.5 nmlpm cm^{-2}), high air flow (100 nmlpm cm^{-2}) followed by a cool-down to room temperature. One typical temperature profile was selected during the load shutdown. The two last conditions are uniform temperatures of 673 and 298 K over the SRU. These steps are referred as SH16-18.

The inlet conditions that were fixed for all simulations are listed in Table 2. Table 3 lists the values of the current density and potential for steps IV1-LS15, whereas Table 4 provides the maximum thermal gradient and temperature difference for one analysis step per group in the four different thermo-electrochemical cases, i.e. co- and counter-flow configurations and with TPOX reformate or partially steam-reformed methane. Thus, analysis steps IV1-6, LS7-15 and SH16-18 refer to IV characterisation, dynamic variation of the electrical load and rapid load shutdown and cool-down, respectively.

Finally the thermo-electrochemical cases in counter-flow configuration were simulated for the C1 cell with two different initial thicknesses of the gaskets, i.e. a value identical to, or 5% thicker than that of the GDL. They are identified as cases of gasket "no preload" and "preload", respectively. The latter is the default case. Thus, all simulations with the C2 cell included 5% thicker gaskets.

3. Results and discussion

3.1. Probability of failure of the cell at room temperature

The residual stresses in the cell can be easily computed with reasonable accuracy by simple models [42]. For instance, it has been often reported [41] that in the anode-supported cell, the support is subjected to tensile stresses, while both the electrolyte and the LSM-YSZ cathode are submitted to compressive stresses, since their CTE is smaller than the one of the anode. The computations performed in the current study show the same trend for both the C1 and C2 cells.

Fig. 5 depicts the evolution of the probability of failure at room temperature for the two different types of cells and initial thickness of the gaskets in the following states: as sintered and unconstrained (INI1), after the assembly (INI2), and after a cool-down in reduced state (SH18), which would correspond to a first thermal cycle. Only the anode contributes to the probability of failure, since the other layers undergo compressive stresses. A cool-down in reduced state (SH18) is critical for the C1 and C2 cells. This is due to the reduction strain, the larger CTE and the decrease in strength of the anode support, induced by the higher porosity in the reduced state, which is not completely compensated by the corresponding decrease in Young modulus.

A prediction of the model that may induce disagreement with common experimental observations is the decrease of the probability of failure during the assembly for both the C1 and C2 cells.

Table 3
Values of current density and voltage for steps IV1-LS15.

	TPOX reformate				Partially steam-reformed methane			
	Co-flow		Counter-flow		Co-flow		Counter-flow	
	U (V)	j (A cm^{-2})	U (V)	j (A cm^{-2})	U (V)	j (A cm^{-2})	U (V)	j (A cm^{-2})
IV1	1.00	0.00	1.00	0.00	0.97	0.00	0.99	0.00
IV2	0.89	0.10	0.89	0.10	0.81	0.10	0.89	0.10
IV3	0.82	0.20	0.82	0.20	0.77	0.20	0.84	0.20
IV4	0.76	0.30	0.77	0.30	0.75	0.30	0.81	0.30
IV5	0.67	0.40	0.69	0.40	0.73	0.40	0.77	0.40
IV6	0.62	0.42	0.66	0.42	0.71	0.44	0.75	0.44
LS7	0.82	0.23	0.87	0.15	0.79	0.05	0.74	0.37
LS8	0.74	0.38	0.75	0.37	0.65	0.42	0.78	0.36
LS9	0.71	0.39	0.75	0.37	0.75	0.37	0.82	0.34
LS10	0.70	0.40	0.72	0.38	0.79	0.35	0.84	0.21
LS11	0.79	0.22	0.80	0.22	0.79	0.35	0.84	0.21
LS12	0.84	0.12	0.85	0.12	0.83	0.21	0.86	0.18
LS13	0.78	0.29	0.81	0.22	0.86	0.12	0.87	0.12
LS14	0.72	0.38	0.72	0.38	0.80	0.35	0.82	0.34
LS15	0.70	0.40	0.72	0.39	0.76	0.36	0.81	0.34

Table 4
Representative values for each group of analysis steps of the structural analysis.

	TPOX reformate						Partially steam-reformed methane					
	Co-flow			Counter-flow			Co-flow			Counter-flow		
Analysis step	IV5	LS8	SH16	IV5	LS8	SH16	IV5	LS8	SH16	IV5	LS8	SH16
Max. local current density (A cm^{-2})	0.56	0.60	–	0.81	0.68	–	0.56	0.68	–	0.75	0.48	–
Max. thermal gradient (K m^{-1})	1988	3221	805	1548	2062	812	1948	1743	1030	1239	2332	711
Max. temperature difference (K)	126	163	105	132	173	95	144	130	105	109	120	78

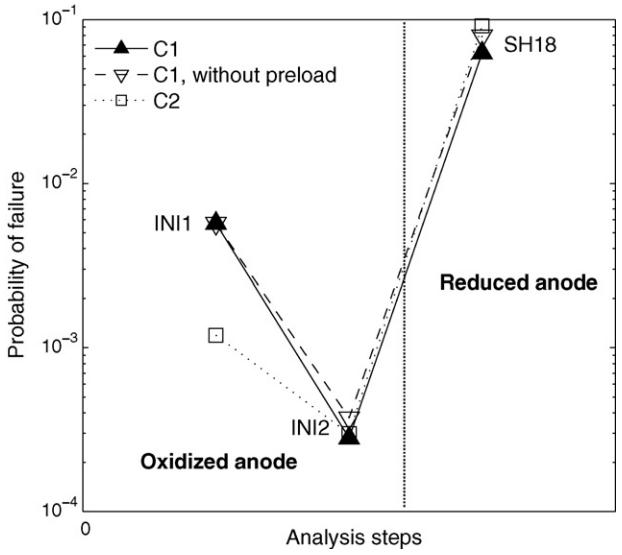

Fig. 5. Probability of failure at room temperature for the two different types of cell, with and without gasket preload.

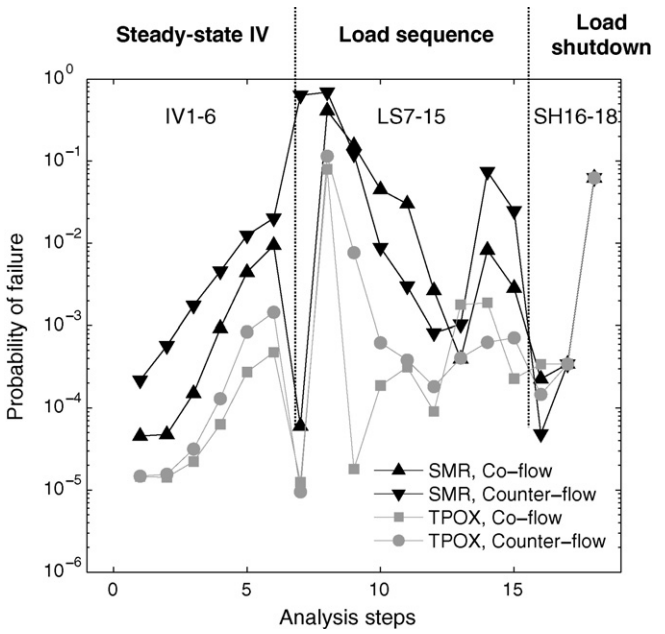

Fig. 6. Probability of failure in the C1 cell for the four thermo-electrochemical cases.

Indeed, the model indicates that the flattening of the cells lowers the magnitude of the maximum tensile stress at the interface between the anode and the electrolyte. This effect is obviously more pronounced for the C1 cell, as a result of the absence of a compensating layer. Failures experimentally observed during assembly are more likely related to the quality of the components: a stiff GDL of poor quality, for instance, can induce very high local stresses. Such phenomena were not modelled and are expected to be negligible if foams – as in the present work – or components of proper quality are used. In addition, the fuel side of the anode is in compressive state when the cell is unconstrained. In the case of the C1 cell, the stresses turn from compressive to tensile in this location during the assembly. Therefore, failure can arise from defects that did not initiate fracture due to the compressive stress. The influence of the gasket preload is limited, but surprisingly beneficial in terms of reduced probability of failure (decrease down to 1.7E−2). Indeed, it limits the bending of the cell in the area between the gaskets, hence the magnitude of the probability of failure.

3.2. Probability of failure of the cell during operation

The evolution of the probability of failure during operation is depicted in Fig. 6 for the C1 cell, and the four thermo-electrochemical cases. The trend is quite similar for all cases independent of the flow configuration or fuel type. The probability of failure first increases during the current–voltage characterisation (IV1-6). The highest probabilities are reached during transient operation (LS8) and are significantly larger than the ones related to both thermal cycling (SH18) and steady-state operation at nominal load (IV5).

This difference between nominal (IV5) and transient operation (LS8) is more pronounced in the co-flow configuration. Indeed, the margin to accommodate severe conditions during transient operation is less for an equivalent performance, compared to the counter-flow case. This applies for operations with both TPOX reformate and partially steam-reformed methane. In comparison, the rapid load shutdown procedure does not induce particular harmful conditions for the cell in both co- and counter-flow configurations.

The first principal stress in the anode of the C1 cell and the corresponding temperature profile are displayed in Fig. 7 to provide more insights into the reason for the significant increase of the probability of failure during transient operation and the difference between the four thermo-electrochemical cases. The selected operating conditions refer to the highest probability of failures for each thermo-electrochemical case, namely analysis step LS8. In Fig. 7, the MIC is depicted in transparency and the deformation highly exaggerated (factor of 100) to appreciate the stresses around the fuel manifold as well. It is observed that the zones of relatively high temperature located mainly in the area of highest current density induce large tensile stress at the sides and the air outlet of the anode support and induces a slight release of the compressive stresses in the electrolyte. The comparison between the temperature profiles at the nominal point (IV5) and most critical conditions (LS8) (middle and right column, respectively in Fig. 7) highlights how a zone of relatively higher temperature can develop during transient operation and so a corresponding increase in the probability of failure. This phenomenon is particularly pronounced when the SRU is operated in counter-flow configuration and fed with partially steam-reformed methane (LS7). Indeed, the decrease of temperature induced by the steam-reforming reaction and the air inlet acts on opposite sides: during the transient from idle to full load, the zone of highest current density is located in the middle of the active area of the SRU. In these conditions, the control of the air flow on the air outlet temperature is not ideal, since the controller cannot prevent the large temperature overshoot in the middle of the SRU. Unfortunately, local temperature measurements are very difficult to implement in large stacks and thus seldom available. The same reasoning explains the differences between the four thermo-electrochemical cases: internal steam-methane reforming and counter-flow induce more harmful conditions than thermal partial oxidation and co-flow, respectively. Unfortunately, the opposite applies for the cell performance.

Some researchers used the maximum absolute value of the thermal gradients to assess the risks encountered by the cell during dynamic simulations or fixed operating point [43]. The results of the present study show that such criterion is not fully reliable. Plotting the probability of failure against the maximum temperature difference or thermal gradient over the SRU does display a weak correlation (see Fig. 8). But, particular care is required when using thermal gradients or temperature profiles as an indicator for cell failure. Indeed, a fixed value of maximum thermal gradient or temperature profile can correspond to a wide range of probability of

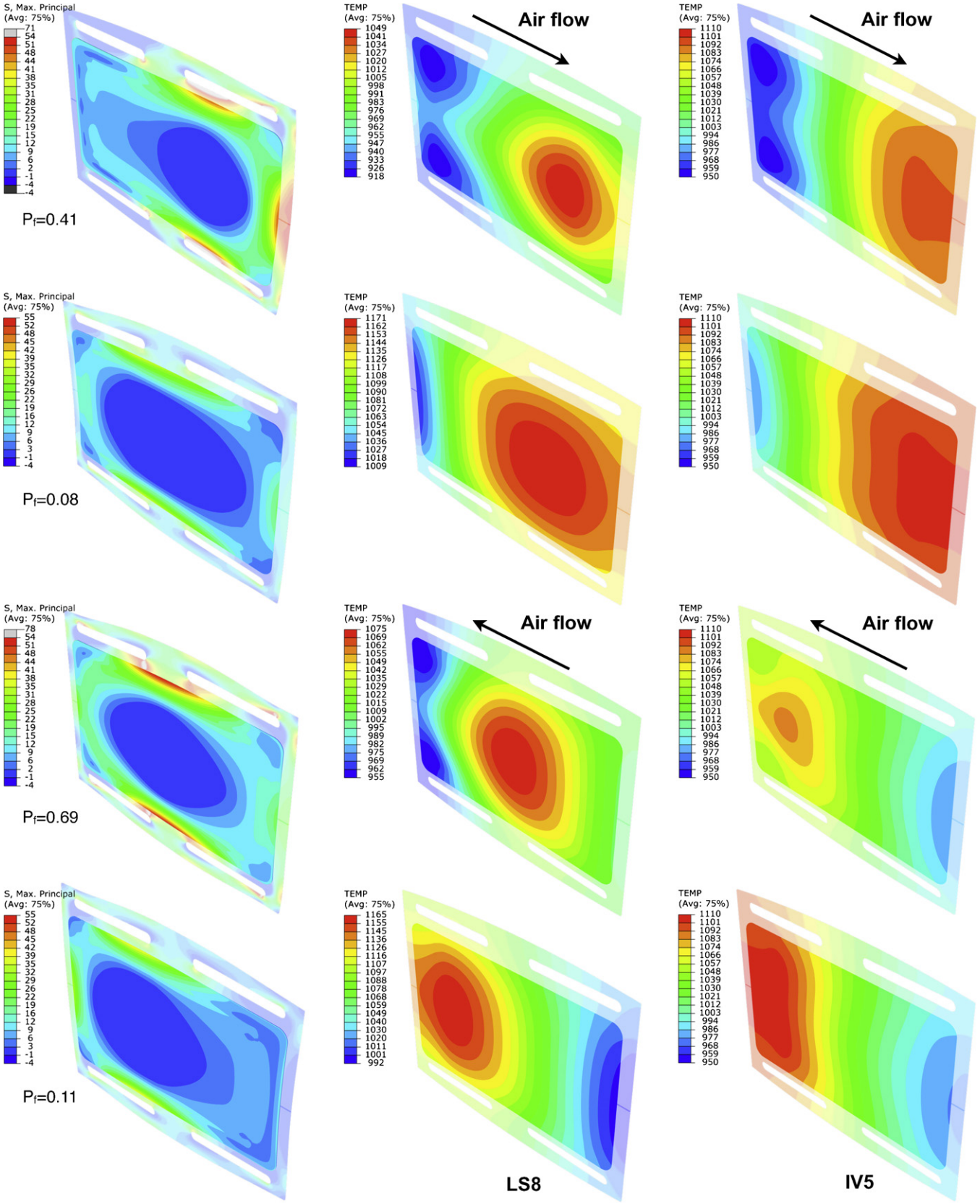

Fig. 7. 1st principal stress (MPa) in the anode (left) and corresponding temperature (middle) for the most critical analysis steps (LS8), in term of cell failure. The temperature profiles at nominal point (IV5) are depicted for comparison (right). Internal steam-methane reforming, co-flow configuration (top), TPOX, co-flow configuration (second), internal steam-methane reforming, counter-flow configuration (third), TPOX, counter-flow configuration (bottom).

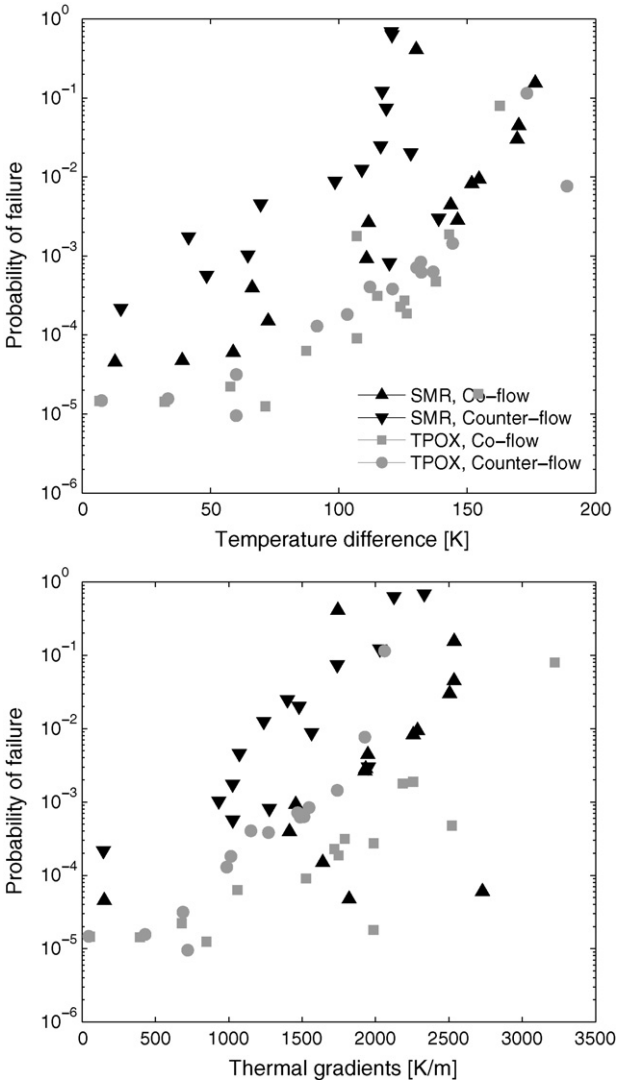

Fig. 8. Correlation between probability of failure and temperature difference (top) and thermal gradients (bottom) over the SRU. C1 cell, IV1-LS15.

failure, which overlaps more than two orders of magnitude. Thus, such a correlation holds imperfectly only for a given design, under fixed operating conditions and flow configuration. Hence, structural analysis is required prior to the use of a simple criterion. The shape of the temperature profile and location of the thermal gradient within the components of the repeat element play an important and combined role.

During operation, as at room temperature, the anode is the only layer, which undergoes tensile stresses and which explains the difference in probability of failure between the two cell types (see Fig. 9): the compensating layer in the C2 cell induces slightly more stress in the anode. The magnitude is small compared to the effect of the operating conditions. Unlike the room temperature case, the application of a preload on the gaskets is slightly less favourable. The contribution of the residual stresses decreases with increasing temperature. Therefore, the effect of the limitation of the bending induced by gasket preload is less pronounced. The maximum difference of 5.85E−3 occurs when the SRU is fed with partially steam-reformed methane and operated in counter-flow configuration. In addition, the mismatch in CTE between the GDLs and the gaskets induces slightly higher tensile stresses in these locations.

Fig. 10 provides the details of the contributions to the probability of failure in the C1 cell in counter-flow configuration, when the

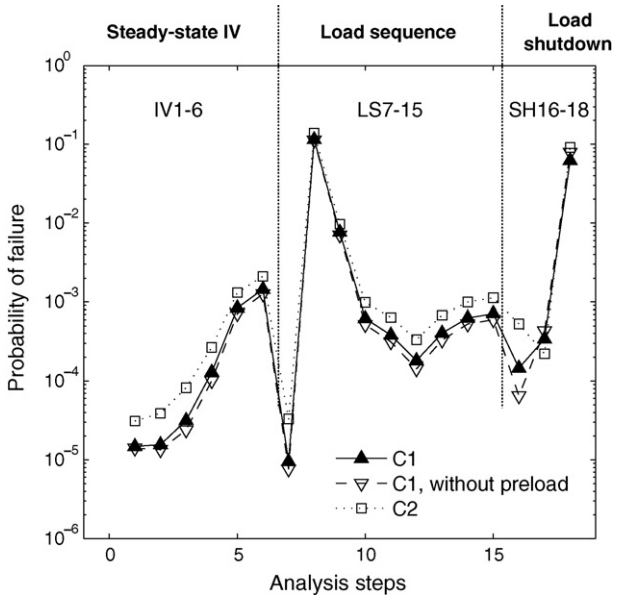

Fig. 9. Probability of failure for the two different cells with (C1 and C2) or without (C1) preload on the gaskets. TPOX reformate, counter-flow configuration. The trend is similar when the cell is fed with partially steam-reformed methane and counter-flow configuration.

SRU is fed with partially steam-reformed methane. The error bars cover the variation corresponding to the 95% confidence interval in the ring-on-ring strength test data. Confidence intervals were provided only for the anode layer [12]. The lowest probabilities of failures correspond to the most favourable case, i.e. highest Weibull modulus and characteristic strength. The computed values overlap several orders of magnitude. The trends can be detected satisfactorily, but design with such information is hazardous, and ideally as much samples as possible should be used to obtain more reliable data.

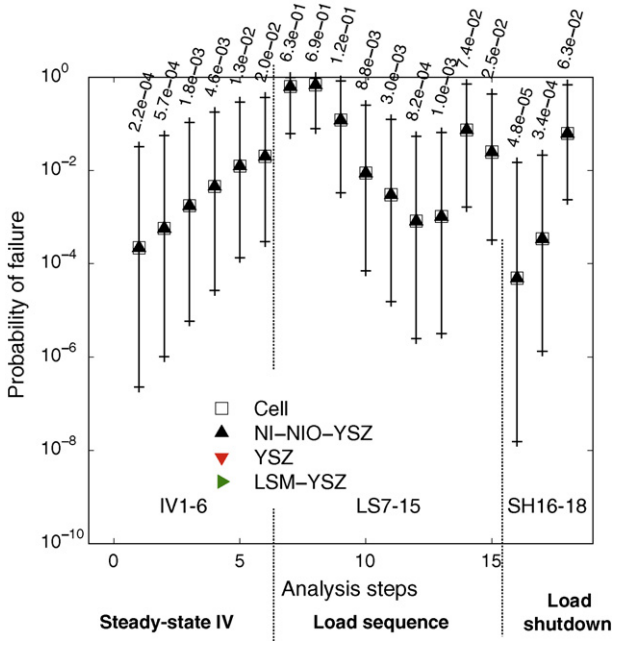

Fig. 10. Contributions to the probability of failure of the cells and scatter induced by the 95% confidence interval. C1 cell, partially steam-reformed methane, counter-flow configuration.

Table 5
Probability of failure for a 50-cell stack.

	Co-flow		Counter-flow	
	5 cells	50 cells	5 cells	50 cells
TPOX reformate				
Step IV5	1.4E−3 (1.3E−1, 2.2E−6)	1.4E−2 (7.6E−1, 2.2E−5)	4.2E−3 (2.3E−1, 1.5E−5)	4.1E−1 (9.3E−1, 1.5E−4)
Step LS8	3.4E−1 (1, 8.7E−3)	9.8E−1 (1, 8.4E−2)	4.6E−1 (1, 1.6E−2)	1 (1, 1.5E−1)
Partially pre-reformed methane				
Step IV5	2.2E−2 (5.9E−1, 1.4E−4)	2E−1 (1, 1.4E−3)	6.1E−2 (8.3E−1, 6.7E−4)	4.7E−1 (1, 6.7E−3)
Step LS8	9.3E−1 (1, 1.2E−1)	1 (1, 7.1E−1)	1 (1, 3.4E−1)	1 (1, 9.8E−1)

The probability of failure of a single repeat element is of little interest. Table 5 summarizes the probability that one cell fails in a 50-cells stack at the nominal (IV5) and most critical (LS8) point. Overall, the probabilities are critical for a product. The uncertainty induced by the 95% confidence interval is tremendous. The computed probabilities are more reasonable if the most favourable set of Weibull parameters is used, which represent for the anode a change from 79.1 to 85.4 MPa in characteristic strength and 7.0–10.1 in Weibull modulus. The difference between the most critical case (LS8) and the nominal operating point (IV5) is significant. Thus, improper control strategy or failures of auxiliary components are believed to provoke rapidly harmful conditions. As a matter of fact, the load sequence simulated in the present study is not even very severe [22], since all devices, e.g. PID and mass flow controllers and sensors were assumed to work flawlessly.

3.3. Requirements on material properties

Typical required probabilities of failure for devices for stationary application are in the range of 10^{-5}. The strength of ceramics is not a material property, since it depends on the manufacturing process, which might either induce or prevent critical defects. It is therefore foreseen that the reliability can be enhanced by material improvements. A decrease of the probability of failure can be achieved by increasing either the Weibull modulus or the characteristic strength. Figs. 11 and 12 depict the combinations of modulus and characteristic strength that ensure a probability of survival of 0.99 in a 50-cell stack, which can be considered suitable for a prototype. It should be emphasized that such plots are valid only for a fixed reference volume and thus ring-on-ring measurement

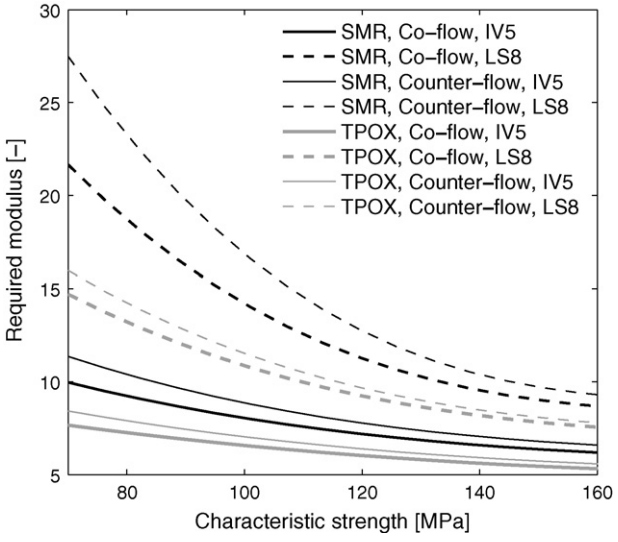

Fig. 11. Comparison between the requirement on the strength of the anode material for the C1 cell, for the four different thermo-electrochemical cases to ensure a probability of failure of 10^{-2} in a 50-cells stack.

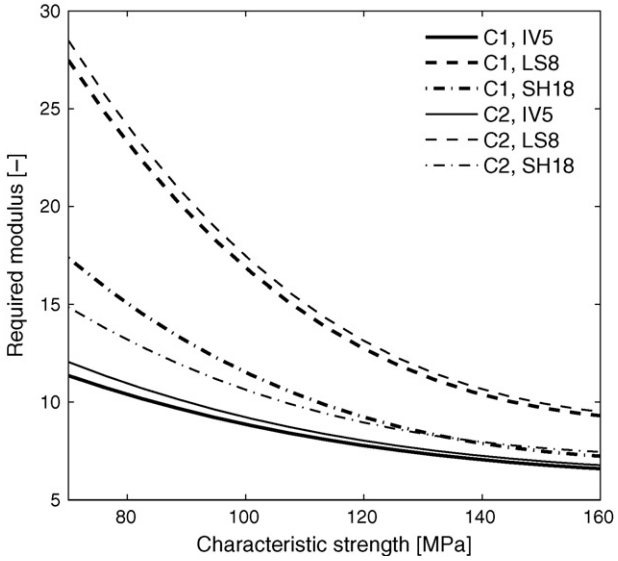

Fig. 12. Comparison between the requirement on the strength of the anode material for the two types of cells to ensure a probability of failure of 10^{-2} in a 50-cell stack. Partially steam-reformed methane, counter-flow configuration.

device. The first figure focuses on the comparison between steady-state (IV5) and most critical (LS8) for the C1 cell, whereas the second compares the C1 and the C2 cell, all with gasket preload. The requirements for steady-state operation are reasonable, independently of the fuel, flow configuration or type of cell. A value of 10 for the Weibull modulus is often mentioned as a requirement for technical ceramics. It would achieve the targeted probability of survival for the C1 cell, combined to fairly high strengths of 90 MPa at 1073 K and reduced state, which lies slightly above the 95% confidence interval of the data measured at room temperature used in the present study. On the contrary, transient operation is much more demanding. It is very challenging to achieve such drastic improvements in the mechanical properties of the anode material. Instead, a suitable control strategy, which does not focus exclusively on performance or availability but on reliability as well, is then of paramount importance.

4. Conclusion

Coupling a detailed thermo-electrochemical model to a finite-element tool enabled the structural analysis of a SOFC stack of latest generation developed within the frame of the FP6-FLAMESOFC projects at LENI-EPFL in collaboration with HTcearmix-SOFCPower. All components of a single representative repeat unit were meshed and their interactions modelled through contact simulations.

The probabilities of failures for the cell were computed for each layer from a detailed sub-model coupled to the SRU contact model. In both the C1 and C2 types of cell, only the anode contributed to the probability of failure at both room and operating temperature. In

the former case, residual stresses due to the manufacturing process, combined to the reduction strain and the decrease of the strength of the reduced anode material revealed the cool-down as a critical situation. The model predicted a decrease of the probability of failure during the assembly, which is not consistent with experimental observations. One reason for the discrepancy is likely the presence of local defects in the components, which were not modelled.

The most harmful operating conditions were found to occur during transient operation and induced higher probabilities of failure in the counter-flow configuration, when the SRU is fed with partially steam-reformed methane. Tensile stresses in the anode were generated around the zones of locally highest temperature. The latter were found to be possibly promoted more significantly and in a different form during the variations of the electrical load than during steady-state (i–V) calculations. As a general trend, thermal partial oxidation and co-flow configuration were found more favourable than internal steam reforming and counter-flow respectively, the trend is opposite for the cell performance. However, co-flow configuration can be potentially more prone to sudden failure during transient operation.

Thermal gradient and temperature differences over the SRU can be used in a limiting and careful manner to assess the risks related to a temperature profile. Nevertheless, the indicators are valid only for a given design and thermo-electrochemical case. Hence, structural analysis cannot be neglected.

The computed probabilities of failure of a 50-cell stack were unacceptable for a product. However, the source used for the Weibull parameters included a limited number of samples in ring-on-ring experiments. Computed values changed significantly if a more favourable set of parameters within the 95% confidence interval was used. Considering the problem from a material point a view, the requirements were acceptable for steady-state operation but beyond the range of foreseen possible improvements of the anode material during transient operation. The need for a suitable control strategy is thus highlighted.

Acknowledgements

This work was funded by the FP6 FLAMESOFC European project; contract number CE-Flame SOFC-019875, the Swiss Consortium, co-financed by the Swiss Federal Office of Energy (SFOE), contract number 152210 and Swisselectric Research. The author A.N. would like to thank Dr. Joël Cugnoni (EPFL-LMAF) for his valuable advices during the development of the contact model. Patrick Metzger from DLR is kindly acknowledged for the experimental data on his segmented test rig. A.N. furthermore thanks Dr. Ulrich Vogt and Dr. Jakob Kübler from EMPA, Switzerland, for their advices on the material properties. Simulation were carried out with gPROMS® a product of Process Systems Enterprise Limited and ABAQUS under academic licensing on the Pleiades2 cluster located at EPFL.

References

[1] Z. Wuillemin, N. Autissier, A. Nakajo, M.-T. Luong, J. Van Herle, D. Favrat, Fuel Cell Sci. Technol. 5 (1) (2008) 011016–011019.
[2] D. Sarantaridis, R.A. Rudkin, A. Atkinson, J. Power Sources 180 (2008) 704–710.
[3] H. Yakabe, I. Yasuda, J. Electrochem. Soc. 150 (1) (2003) A35–A43.
[4] H. Yakabe, T. Ogiwara, M. Hishinuma, I. Yasuda, J. Power Sources 102 (2001) 144–154.
[5] H. Yakabe, Y. Baba, T. Sakurai, J. Power Sources 135 (2004) 9–16.
[6] H. Yakabe, Y. Baba, T. Sakurai, J. Power Sources 131 (2004) 278–284.
[7] A. Selimovic, M. Kemm, T. Torisson, M. Assadi, J. Power Sources 145 (2005) 463–469.
[8] C.-K. Lin, T.-T. Chen, Y.-P. Chyou, L.-K. Chiang, J. Power Sources 164 (2007) 238–251.
[9] A. Nakajo, C. Stiller, G. Härkegard, O. Bolland, J. Power Sources 158 (2006) 287–294.
[10] A. Atkinson, A. Selçuk, Acta Mater. 47 (3) (1999) 867–874.
[11] A. Atkinson, A. Selçuk, Solid State Ionics 134 (2000) 59–66.
[12] M. Radovic, E. Lara-Curzio, Acta Mater. 52 (2004) 5747–5756.
[13] D.L. Meixner, R.A. Cutler, Solid State Ionics 146 (2002) 285–300.
[14] Y.S. Chou, J.W. Stevenson, T.R. Armstrong, L.R. Pederson, J. Am. Ceram. Soc. 83 (6) (2000) 1457–1464.
[15] ThyssenKrupp VDM, Material Data Sheet No. 4046, http://thyssenkruppvdm.de/_pdf/Crofer22APU_e.pdf.
[16] L.J. Gibson, M.F. Ashby, Cellular Solids: Structure & Properties, Pergamon Press, New York, 1988.
[17] M. Bram, S. Reckers, P. Drinovac, J. Mönch, R.W. Steinbrech, H.P. Buchkremer, D. Stöver, J. Power Sources 138 (2004) 111–119.
[18] R. Goodall, C. Williams, J.A. Fernie, T.W. Clyne, et al., Int. SAMPE Symp. Exhibition (Proc.) 47 (II) (2002) 1001–1010.
[19] S.H. Chan, X.J. Chen, K.A. Khor, J. Electrochem. Soc. 151 (1) (2004) A164–A172.
[20] P. Costamagna, P. Costa, V. Antonucci, Electrochim. Acta 43 (1998) 375–394.
[21] B. Kenney, K. Karan, Solid State Ionics 178 (2007) 297–306.
[22] C. Stiller, B. Thorud, O. Bolland, R. Kandepu, L. Imsland, J. Power Sources 158 (2006) 303–315.
[23] A. Nakajo, et al., J. Power Sources 193 (2009) 216–226.
[24] D. Larrain, J. Van herle, F. Maréchal, D. Favrat, J. Power Sources 131 (2004) 304–312.
[25] gPROMS (General Process Modelling and Simulation Tool), v3.0.2, Process Systems Enterprise Ltd., London, http://www.psenterprise.com/.
[26] C. Stiller, B. Thorud, S. Seljebø, Ø. Mathisen, H. Karoliussen, O. Bolland, J. Power Sources 141 (2005) 227–240.
[27] J.H. Park, R.N. Blumenthal, J. Electrochem. Soc. 136 (1989) 2867.
[28] J. Fleig, H.L. Tuller, J. Maier, Solid State Ionics 174 (2004) 261–270.
[29] R.J. Kee, H. Zhu, J. Power Sources 117 (2003) 61–74.
[30] E. Achenbach, E. Riensche, J. Power Sources 52 (1994) 283–288.
[31] W.G. Bessler, J. Electrochem. Soc. 153 (8) (2006) A1492–A1504.
[32] F.H. van Heuveln, H.J.M. Bouwmeester, J. Electrochem. Soc. 144 (1) (1997).
[33] P. Metzger, K.-A. Friedrich, H. Müller-Steinhagen, G. Schiller, Solid State Ionics 177 (2006) 2045–2051.
[34] ABAQUS Inc., v6.7, Hibbitt, Karlsson and Sorensen, Rhode Island.
[35] MATLAB, v7.5, The Mathworks Inc., Natik.
[36] P. Charpentier, P. Fragnaud, D.M. Schleich, E. Gehain, Solid State Ionics 135 (2000) 373–380.
[37] ThyssenKrupp VDM, Material Data Sheet No. 1001, www.thyssenkrupp-vdm-fareast.com/media/down_datasheets_corres_new/nickel_99_2_e.pdf.
[38] A. Selçuk, A. Atkinson, J. Eur. Ceram. Soc. 17 (1997) 1523–1532.
[39] N.Q. Minh, T. Takahashi, Science and Technology of Ceramic Fuel Cells, Elsevier, 1995.
[40] A.C. Müller, A. Krügel, A. Weber, E. Ivers-Tiffée, Materials Research Society Symposium - Proceedings, vol. 756, 2003, pp. 533–538.
[41] J. Laurencin, G. Delette, F. Lefebvre-Joud, M. Dupeux, J. Eur. Ceram Soc. 28 (9) (2008) 1857–1869.
[42] C.H. Hsueh, Thin Solid Films 418 (2002) 182–188.
[43] P. Aguiar, C.S. Adjiman, N.P. Brandon, J. Power Sources 138 (2004) 120–136.